



# Magnetic confinement of dense plasma inside (and outside) stellar coronae

Rose F. P. Waugh ★ and Moira M. Jardine 

*School of Physics and Astronomy, University of St Andrews, North Haugh, St Andrews, Fife, Scotland KY16 9SS, UK*

Accepted 2022 June 15. Received 2022 June 10; in original form 2022 May 5

## ABSTRACT

Magnetic confinement of dense plasma is found in the magnetospheres of both high- and low-mass stars. Trapped material traces the magnetic field structure, often at large distances from the star where the magnetic structure is otherwise difficult to observe. This work looks specifically at rapidly rotating, solar-like stars where this behaviour is well observed in the form of ‘slingshot’ prominences. We have produced a model for generating cooled magnetic loops in equilibrium with a range of coronal magnetic fields. These loops can be used to populate model coronae and confine material at a wide range of heights above the stellar surface. We calculate masses for slingshot prominences for the star AB Doradus that are consistent with observational values. The model produces two types of solution: loops with summits at low heights and tall solutions beyond the co-rotation radius. We show that the low-lying solutions are footpoint heavy and generally follow the shape of the background field. We refer to these as solar-like prominences. The tall solutions are summit heavy and are centrifugally supported. These are the slingshot prominences. These tall solutions can be found within the stellar wind, beyond the closed corona.  $H\alpha$  trails are generated for various coronal field structures with a range of field geometries and coronal extents. Similar  $H\alpha$  trails are produced by a range of global field structures, which implies that magnetic confinement of material should be common in rapidly rotating stars.

**Key words:** stars: low-mass – stars: magnetic field – stars: mass-loss.

## 1 INTRODUCTION

Magnetic fields are known to confine plasma. Magnetic confinement of material in and beyond the corona of stars is seen in both high- and low-mass stars. Work by Petit et al. (2013) classified the coronae of high-mass stars into two categories: ‘dynamical’ and ‘centrifugal’. This classification depends on the relative locations of the Alfvén radius (the furthest extent of the closed-field corona) and the co-rotation radius (beyond which the outward centrifugal force dominates over gravity). Stars with dynamical magnetospheres have the co-rotation radius ( $r_K$ ) outside of the Alfvén radius ( $r_A$ ), and centrifugal magnetospheres are those with  $r_K < r_A$ . Villarreal D’Angelo, Jardine & See (2018) have since applied this to low-mass stars, in which such centrifugal confinement of cool plasma is observed at, or beyond, the co-rotation radius. In their paper the authors argue that this centrifugal confinement would not occur on stars in the dynamical regime since the co-rotation radius (where confinement is observed) lies in the open-field region where there are no closed field lines to provide magnetic support. On the other hand, stars in the centrifugal regime would be expected to exhibit centrifugal confinement, since the coronal field is still closed above the co-rotation radius.

Prominences are one form of magnetic confinement, where condensations of coronal plasma are supported on closed magnetic field lines. They are well observed on the Sun, where they can be

seen off the limb or on-disc as filaments, but are not exclusively solar features. Prominences have been observed on many other stars and many different types of stellar system, from high-mass stars (Landstreet & Borra 1978) to low-mass stars (Cameron & Robinson 1989a; Dunstone et al. 2006a; Vida et al. 2016; Stauffer et al. 2017), binaries (Hall et al. 1990; Watson et al. 2007; Skelly et al. 2010) to single star systems (Leitzinger et al. 2016) and T Tauri stars (Skelly et al. 2008, 2009) to main sequence, like our Sun. ‘Slingshot’ prominences form on rapidly rotating stars, with coronal material being driven into the tops of magnetic loops by the centrifugal force. They were first observed on the star AB Doradus (Cameron & Robinson 1989a,b), which has since become the prototype for studying these features. Slingshot prominences have been observed on other stars, for example, Speedy Mic (Dunstone et al. 2006a,b), HK Aqr (Byrne, Eibe & Rolleston 1996; Van den Oord 1998; Leitzinger et al. 2016), PZ Tel (Barnes et al. 2000; Leitzinger et al. 2016), and LQ Lup (Donati et al. 2000).

Slingshot prominences differ from solar prominences in their mass and extent. They are 10–100 times the mass of solar prominences (Cameron et al. 1999) and on AB Doradus were predicted to have a size around 0.3 times the stellar area (Cameron & Robinson 1989a). On AB Doradus, it is thought that around eight large prominences may exist at any given time in the visible hemisphere (Collier Cameron 1996). Whilst solar prominences form in the corona of the Sun, it is not clear that slingshot prominences form within the stellar coronae. Slingshot prominences have been observed co-rotating with their host stars at distances that are multiple stellar radii above the surface of the star (Cameron & Robinson 1989a,b; Doyle & Cameron

\* E-mail: [rw47@st-andrews.ac.uk](mailto:rw47@st-andrews.ac.uk)

1990; Cameron & Woods 1992; Byrne et al. 1996; Eibe 1998; Barnes et al. 2000; Donati et al. 2000; Barnes et al. 2001; Skelly et al. 2008, 2009; Leitzinger et al. 2016; Kolbin & Tsybal 2017; Cang et al. 2020). That stellar coronae should extend to such large heights above the stellar surface is not a certainty. In fact, the coronae of rapidly rotating stars are instead thought to be compact. Studies by Hussain, Jardine & Cameron (2001), Hussain et al. (2002), and Jardine, Cameron & Donati (2002a,b), which combined X-ray data and surface magnetograms and used field extrapolation methods to couple the surface magnetic field and coronal emission. These suggest that the coronae of these stars are not hugely extended. Not all theoretical models of slingshot prominences require the background magnetic field to be closed however (Jardine & van Ballegoijen 2005; Waugh & Jardine 2019). Recent work by Climent et al. (2020) found radio emission from multiple stellar radii above the surface of AB Doradus. The authors suggested multiple possible explanations for this, including magnetically driven loop structures and helmet streamers. Radio emission from large-scale magnetic structures was also seen by Massi et al. (2008) in the young, binary system V773 Tau A.

Understanding prominences on these rapidly rotating, low-mass stars is important in order to understand their magnetic fields and evolution. Slingshot prominences will be ejected from the star when they become unstable (Villarreal D’Angelo et al. 2018). These large ejections of mass will have consequences for the stellar evolution, as many of these large-scale features will form and be ejected over time. Prominences are largely ignored from stellar evolution models, though they could be contributing significantly to the mass-loss of stars at this point in their life-cycle (Waugh et al. 2021). Alongside mass, prominence ejection would also remove angular momentum, contributing to the spin-down of these stars (Aarnio, Matt & Strassun 2012; Cranmer 2017; Villarreal D’Angelo et al. 2019; Waugh et al. 2021).

Prominences could have uses as tracers of the magnetic field (Collier Cameron, Jardine & Donati 2002), since they form only on closed magnetic field lines. The observation of a prominence at a certain location around the star informs us that the field must be closed there. The magnetic field of a star tells us not only about its current activity levels but also about how the star will evolve through its association with the stellar wind (Weber & Davis 1967; Vidotto et al. 2011). Being able to accurately model the magnetic field structure is therefore very important. Current models of stellar magnetic fields rely on Zeeman Doppler Imaging (ZDI) maps, which provide the magnetic field strength and direction at the stellar surface. This must then be extrapolated into the corona, which requires several assumptions to be made. Firstly, an assumption must be made about the location of the ‘source surface’ – the radius at which the magnetic field becomes purely radial (Reville et al. 2015; See et al. 2018). The location of this source surface for any given star is uncertain. Secondly, an assumption must be made about whether the field is potential or non-potential. Whilst prominence locations may not directly shed light on these assumptions, they may provide crucial details about local field structures within the large-scale field.

Observations of prominences where masses of these features can be predicted can constrain not only the field structure but also the field strengths. With a prominence mass known, predictions can be made about the field strength that would have been required to support this mass (Cameron & Robinson 1989a). Jardine & Cameron (2019) showed that measurements of prominence masses could also be used to measure the wind mass-loss rates. Wind mass-loss rates for cool stars are very difficult to measure due to their low densities.

Yet, the stellar rotational evolution is determined by their winds. Winds for these stars have previously been measured through a range of methods: the thermal radio emission produced (Panagia & Felli 1975) as the wind expands; the wind interacting with the interstellar medium (Wood et al. 2005); or the interaction of a planetary atmosphere with the stellar wind (Bourrier et al. 2016; Vidotto & Bourrier 2017). The former of these methods usually does not provide a wind density but instead yields an upper-limit based on the lack of a detection (Lim & White 1996; Van den Oord & Doyle 1997; Villadsen et al. 2014; Fichtinger et al. 2017). Jardine & Cameron (2019) noted that prominences form on these stars by a wind that blows up the footpoints of loops, similar to the wind on open field lines. At the coronal temperatures of these stars, this wind is supersonic by the time it reaches the prominence formation site. As a result, the surface is unaware of the formation of the prominence. The prominence mass grows with time until it can no longer be supported. It is then ejected, contributing to the stellar mass-loss like an intermittent wind. A new prominence is then formed, and the cycle continues. Measurements of the prominence mass-loss rates therefore give an estimate of the wind mass-loss rates. This is particularly useful since it provides a measurement method for the most active stars, where there are few other measurements.

Despite the multitude of observations, theoretical models are also required to fully understand the locations of prominence formation. Observations of prominences typically involve producing  $H\alpha$  trails (Cameron & Robinson 1989a, b; Cameron & Woods 1992; Byrne et al. 1996; Eibe 1998; Barnes et al. 2000; Donati et al. 2000; Barnes et al. 2001; Skelly et al. 2008, 2009; Leitzinger et al. 2016). When observed in the  $H\alpha$  line, prominences are seen as transiting absorption features as they backscatter starlight out of the observers line of sight. From the slope of these absorption trails, the cylindrical radius of the prominence can be found, though it is difficult to disentangle the spherical radius and prominence latitude from this (Cameron & Robinson 1989a). Theoretical models such as Jardine & Cameron (1991), Jardine & van Ballegoijen (2005), and Waugh & Jardine (2019) start with a prescribed global field structure, before modelling the prominences as cooled loops that are in a mechanical equilibrium within that structure. This can provide insight into the sites in the corona at which prominences may be supported. These models show that prominence bearing loops on rapidly rotating stars could take two forms: solar-like loops and slingshot loops. The solar-like loops lie below the co-rotation radius of the star. Their cool gas will fall back to the stellar surface when they become unstable. The slingshot loops, that form in closed loops with summits above the co-rotation radius, will instead be ejected from the star once they become unstable. Ferreira (2000) presented a model that, rather than finding new equilibria for cooled loops, calculated the stable points within a dipole or quadrupole background field and associated these with locations of prominence formation. This method has since been used in models such as those by Jardine et al. (2001) and Jardine & Cameron (2019), which start with the observed ZDI maps to generate coronal field structures, before modelling the prominence formation sites as mechanical stable points in these fields.

This work builds on the previous study (Waugh & Jardine 2019), adapting a dipole field embedded within the equatorial plane to the more general magnetic field structure of a dipole aligned with the rotation axis. The shapes of prominence bearing loops are investigated, prominence masses predicted and  $H\alpha$  spectra are generated.

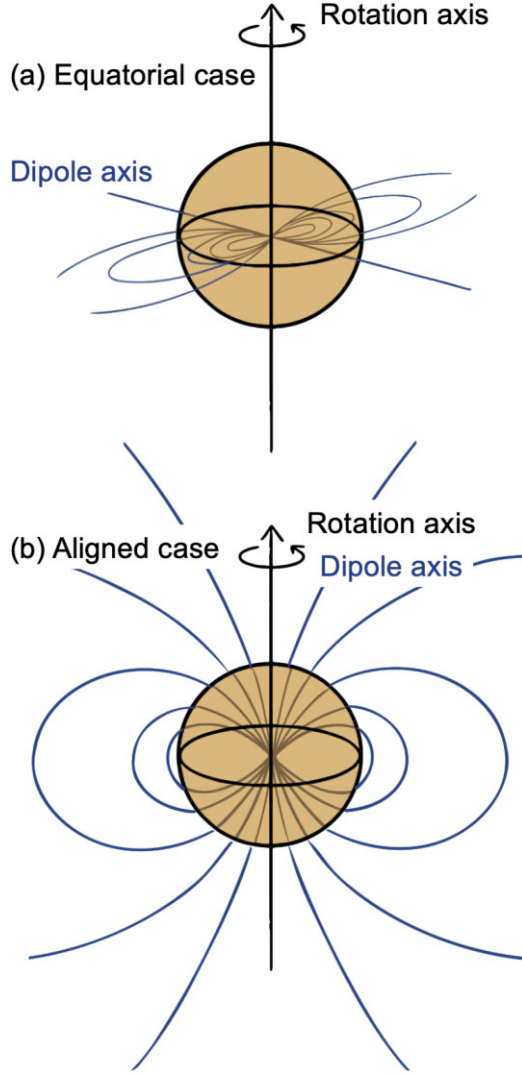


**Figure 1.** Panel (a): a dipole field embedded within the equatorial plane. The field and dipole axes are shown in blue. Panel (b): a dipole field with a dipole axis that is aligned with the rotation axis.

## 2 METHOD

This work expands and generalizes upon the work in Waugh & Jardine (2019) in modelling cooled magnetic loops within a hotter corona. In Waugh & Jardine (2019), the magnetic field was constrained to the equatorial plane of the star. Here we extend the model to solve for loops in meridional planes, i.e. that are aligned with the rotation axis of the star. The magnetic field of the corona is modelled here by a dipole and later by a modified dipole, whose axis is aligned with the rotation axis. The modified dipole is a dipole that opens to radial field at the ‘source surface’ ( $r_s$ ) that can be placed above or below the co-rotation radius of the star. Fig. 1 shows pictorially what we refer to throughout the paper as the ‘equatorial case’ and ‘aligned case’.

The magnetic field structure for the dipole is defined by

$$B_e = B_0 \left( \left( \frac{2 \cos \theta}{r^3} \right) \hat{r} + \left( \frac{\sin \theta}{r^3} \right) \hat{\theta} \right). \quad (1)$$

For a dipole with a source surface, the expression for the field is given by

$$B_e = B_0 \left( \left( \frac{2 \cos \theta}{r^3} \right) \left( \frac{r^3 + 2r_s^3}{R_\star^3 + 2r_s^3} \right) \hat{r} + \left( \frac{\sin \theta}{r^3} \right) \left( \frac{-2r^3 + 2r_s^3}{R_\star^3 + 2r_s^3} \right) \hat{\theta} \right), \quad (2)$$

where  $R_\star$  is the radius of the star,  $B_0$  is the field strength at the stellar surface, and the subscript ‘e’ signifies that this is the ‘external’ field i.e. the global coronal field. We prescribe the temperature of this global corona to be  $T_e = 10^7$  K, with the corona being assumed to be isothermal. The equation of state is given by

$$p = \rho \frac{K_B T}{m}, \quad (3)$$

where  $p$  represents the gas pressure,  $\rho$  is the density,  $K_B$  is the Boltzman constant, and  $m$  is the mean molecular mass.

We assume that the ‘thin flux tube approximation’ holds (Parker 1975; Spruit 1981), such that quantities such as gas pressure and density do not vary across the width of a flux tube, and that the cooled flux tube does not disturb the external field (i.e. its area is less than the pressure scaleheight). This leads to the expression

$$B_i^2 = B_e^2 + 2\mu(p_e - p_i) \quad (4)$$

since the cooled ‘internal’ loop (denoted by the subscript  $i$ ) must be in pressure balance with the external environment. Here  $\mu$  denotes the permeability of free space. This expression can be scaled to units of the base external field strength, and cast in terms of the external plasma beta ( $\beta = B_{0e}^2 / (2\mu p_{0e})$ ):

$$\frac{B_i^2}{B_{0e}^2} = \frac{B_e^2}{B_{0e}^2} + \beta \left( \frac{p_e}{p_{0e}} - \frac{p_i}{p_{0e}} \right). \quad (5)$$

### 2.1 Finding the shapes of prominence bearing loops by force balance

The shape of cooled (prominence bearing) loops is calculated from force balance. The momentum equation for a fluid under the force of gravity and magnetic forces is given by

$$\mathbf{0} = -\nabla p + (\mathbf{j} \times \mathbf{B}) + \rho \mathbf{g}, \quad (6)$$

where the magnetic force can be split into the magnetic tension and pressure forces:

$$\mathbf{0} = -\nabla p + (\mathbf{B} \cdot \nabla) \frac{\mathbf{B}}{\mu} - \nabla \left( \frac{B^2}{2\mu} \right) + \rho \mathbf{g}. \quad (7)$$

Here we formulate the equations in the co-rotating frame and thus the gravitational force is replaced by the ‘effective gravity’, which combines the gravitational and centrifugal forces:

$$\mathbf{g}_e = \left( -\frac{GM_\star}{r^2} + \omega^2 r \sin^2 \theta \right) \hat{r} + \left( \omega^2 r \sin \theta \cos \theta \right) \hat{\theta}, \quad (8)$$

where  $\omega$  represents the stellar rotation rate,  $M_\star$  is the stellar mass, and  $G$  is the gravitational constant.

Equation (7) can be decomposed into components along ( $\hat{s}$ ) and perpendicular ( $\hat{n}$ ) to the field line. These unit vectors are

$$\hat{s} = \frac{1}{\sqrt{r^2 + (r')^2}} (r', r) \quad (9)$$

and

$$\hat{n} = \frac{1}{\sqrt{r^2 + (r')^2}}(-r, r'). \quad (10)$$

Here,  $r'$  represents the derivative of  $r$  with respect to  $\theta$ , i.e.  $r' = dr/d\theta$ .

Along the magnetic field, the momentum equation can be simplified to:

$$0 = -\nabla p \cdot \hat{s} + \rho \mathbf{g}_e \cdot \hat{s}, \quad (11)$$

since the Lorentz force is equal to zero. This can be solved to find the gas pressure variation with  $r$  and  $\theta$ , in terms of the loop temperature ( $T$ ) and base pressure ( $p_0$ ):

$$p = p_0 \exp \left[ \frac{m}{K_B T} \left( G M_\star \frac{(1-r)}{r R_\star} + \omega^2 R_\star^2 \sin^2 \theta \frac{(r^2-1)}{2} \right) \right]. \quad (12)$$

Here  $r$  in equation (12) has been scaled to units of the stellar radius. This expression can be used to solve for both the internal and external field. This is given in more detail in the appendix.

Perpendicular to the field line, the momentum equation is

$$0 = -\nabla p \cdot \hat{n} + \left( B_i^2 \frac{\partial \hat{s}}{\partial s} \right) \cdot \hat{n} - \nabla \left( \frac{B_i^2}{2\mu} \right) \cdot \hat{n} + \rho \mathbf{g}_e \cdot \hat{n}. \quad (13)$$

The first expression in equation (13) can be evaluated to

$$-\nabla p \cdot \hat{n} = \frac{1}{\sqrt{r^2 + (r')^2}} \left( \frac{\partial p}{\partial r} r - \frac{r'}{r} \frac{\partial p}{\partial \theta} \right). \quad (14)$$

The second two expressions in equation (13) combined can be evaluated to

$$(\mathbf{j} \times \mathbf{B}_i) \cdot \hat{n} = \frac{B_i^2 (r r'' - r^2 - 2(r')^2)}{\mu(r^2 + (r')^2)^{3/2}} + \frac{1}{2\mu \sqrt{r^2 + (r')^2}} \left( r \frac{\partial B_i^2}{\partial r} - \frac{r'}{r} \frac{\partial B_i^2}{\partial \theta} \right),$$

and the final expression in equation (13) can be evaluated to

$$\rho \mathbf{g}_e \cdot \hat{n} = \frac{\rho}{\sqrt{r^2 + (r')^2}} \left( \frac{G M_\star}{r} - \omega^2 r^2 \sin^2 \theta + \omega^2 r r' \sin \theta \cos \theta \right). \quad (15)$$

Combining these and simplifying leaves

$$\begin{aligned} & \frac{2r B_i^2 (r^2 + 2(r')^2 - r r'')}{(r^2 + (r')^2)} \\ &= - \left( r^2 \frac{\partial B_i^2}{\partial r} - r' \frac{\partial B_i^2}{\partial \theta} \right) + \left( \frac{\partial p}{\partial r} r^2 - r' \frac{\partial p}{\partial \theta} \right) \\ &+ 2\mu r \rho \left( \frac{G M_\star}{r} - \omega^2 r^2 \sin^2 \theta + \omega^2 r r' \sin \theta \cos \theta \right), \end{aligned} \quad (16)$$

where

$$\rho = \frac{m}{K_B T_i} p \quad (17)$$

and  $p$  is given by equation (12) for the internal gas pressure.  $B_i$  is given by equation (4). Equation (16) can be solved for the shape of the field line  $r(\theta)$  using the expression for the pressure variation with height (equation 12).

'Height-width' plots can be plotted in the same manner as in the previous paper (Waugh & Jardine 2019), where 'height' refers to the radius of the loop summit and 'width' refers to angular distance between the loop summit and a field line footpoint on the stellar surface.

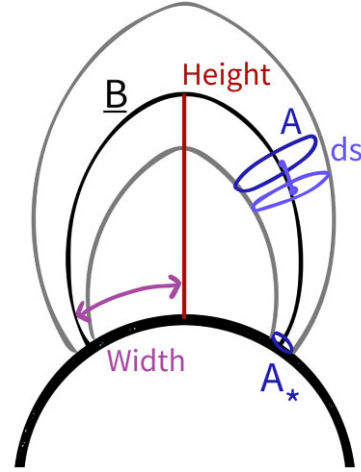


**Figure 2.** Cartoon showing a field line (black) and the surrounding flux tube (grey). The area of the flux tube ( $A$ ) and length of tube elements ( $ds$ ) are shown, alongside definitions of loop height and width.

## 2.2 Calculating prominence mass distributions

The mass of a prominence supported will vary with the loop summit height. This is caused by a combination of the gas pressure and loop volume both varying with loop summit height. The solutions from equation (16) give the shapes of individual field lines and in order to calculate a prominence mass, a flux tube must be constructed around this field line.

From one field line, a flux tube can be defined around it using flux conservation,

$$B_\star A_\star = B(r) A(r), \quad (18)$$

where  $A_\star$  is the area of the flux tube at the stellar surface i.e. base of the loop. This was fixed at 1 per cent of the stellar surface in this work, as in Jardine & Cameron (2019). This allows for the area of the flux tube to be calculated at all points along the field line. The mass at each point along the flux tube is found by multiplying the density at each location on the field line by the volume element of the tube (calculated by  $A ds$ ). The total mass within a flux tube is then the sum of these individual flux tube elements.

## 3 LOOP SHAPES

In this first section, we compare the results of this generalized model with results of the more simplified equatorial model in the previous paper.

### 3.1 Pressure distribution within the corona

The pressure distribution within the corona is determined by equation (12). In the previous paper (Waugh & Jardine 2019), when only the equatorial plane was examined, the pressure distribution varied only with  $r$  and did not depend on  $\phi$ , as shown in equation (19). However, with the dipole axis aligned with the rotation axis, the gas pressure variation depends on  $r$  and  $\theta$ , due to the centrifugal term in the effective gravity:

$$p = p_0 \exp \left[ \frac{m}{K_B T_e} \left( -\frac{G M_\star}{r} \left( 1 - \frac{r}{R_\star} \right) + \frac{\omega^2}{2} (r^2 - R_\star^2) \right) \right]. \quad (19)$$

This can be seen in Fig. 3. In both cases, the pressure decreases with distance from the stellar surface, reaching a minimum at the



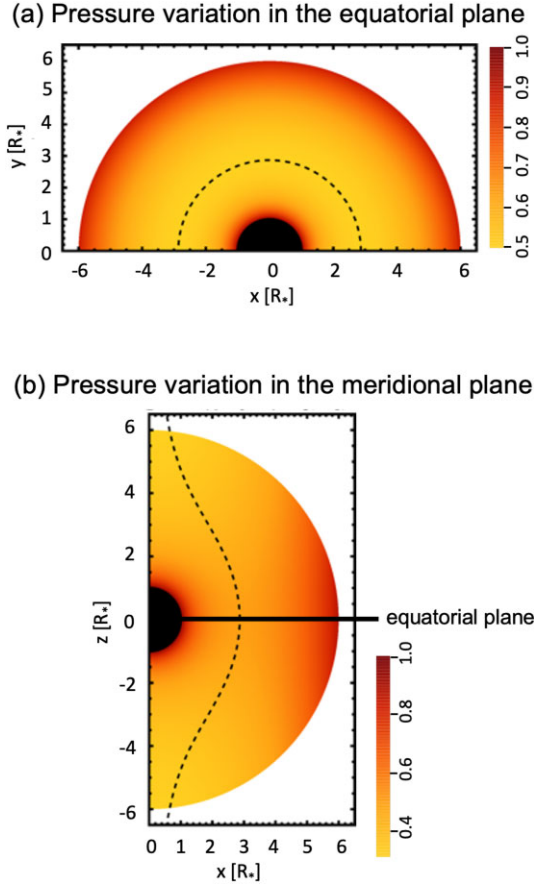


**Figure 3.** Plots showing how the gas pressure varies for (panel a) a dipole whose axis lies in the equatorial plane and (panel b) a dipole whose axis is aligned with the rotation axis. The colour scale is in units of the base pressure in both cases. The black dashed line represents the co-rotation radius of the star and the star itself by the black circle.

co-rotation radius (where the effective gravity is zero since the centrifugal and true gravity are equal). Beyond this radius, the gas pressure increases again. It is at this point that the difference between the equatorial case and the aligned case is most apparent. In the equatorial case, the gas pressure is constant at a fixed  $r$  since circles of fixed  $r$  are equipotentials of the effective gravity term. However, within meridional planes, the gas pressure varies with latitude, as the centrifugal term within the effective gravity drives pressure at large heights down towards the equatorial plane.

### 3.2 Comparison of a dipole within the equatorial plane and a dipole aligned with the rotation axis

This difference in pressure distribution alters the shape of the cooled loops between the equatorial and aligned cases. The overall behaviour, however, has not altered. Example loop shapes and height–width curves are shown in Fig. 4 for the aligned case and the equatorial case. The height–width plots shown in panel (b) of these figures are remarkably similar between the equatorial (purple) and aligned (blue) cases, with deviation only occurring at large heights above the surface. This is when the difference in the pressure distribution between the two cases is most apparent and able to alter the loop shape. In the aligned case, the maximum pressure at a fixed radius is found within the equatorial plane, seen in Fig. 3. Moving away from the equatorial plane at a fixed radius results in a drop in

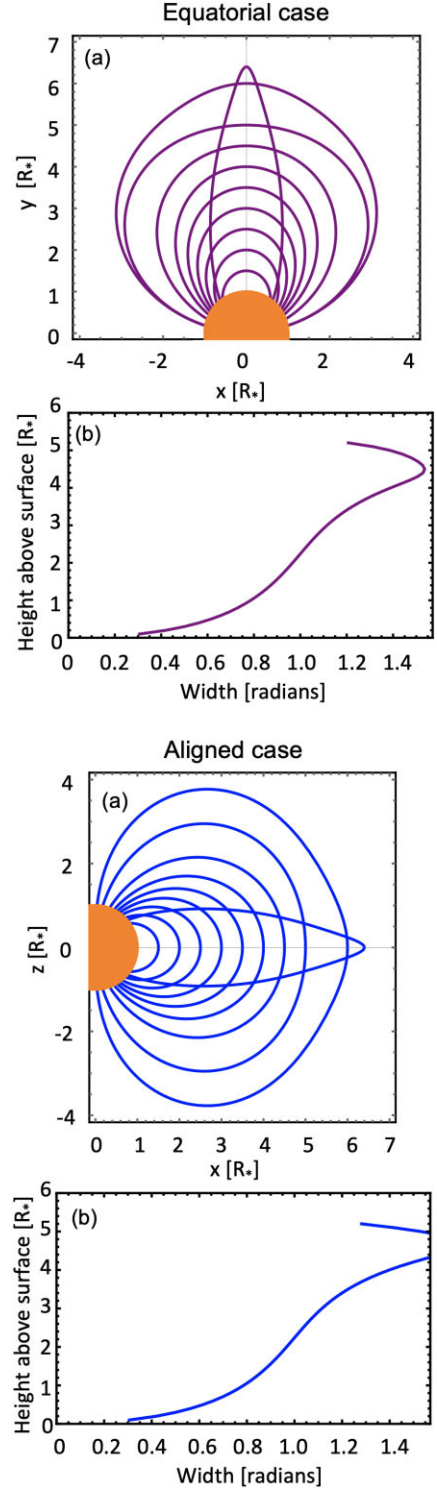


**Figure 4.** Panel (a): example cool loop shapes embedded within a dipole external field. The stellar surface is shown in orange. Panel (b): the height–width curve for these families of solutions. The parameters used here are  $p_{0i}/p_{0e} = 1$ ,  $T_e = 8.57 \times 10^6 \text{ K}$ ,  $T_i = T_e/10$ ,  $\beta = 10^{-4}$ , and AB Dor stellar parameters.

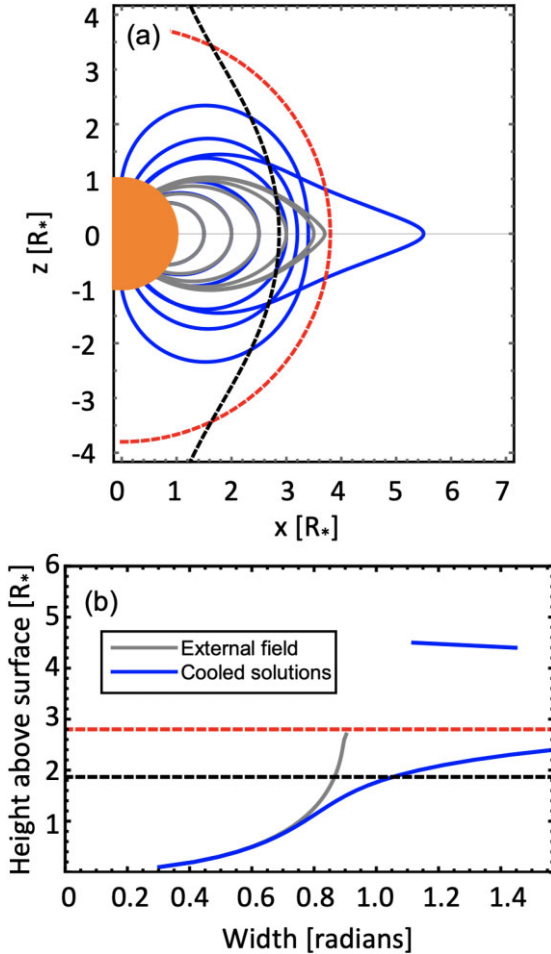


**Figure 5.** Panel (a): example loop shapes for the cooled solutions (blue) and external field (grey). Panel (b): the height–width curve for these families of solutions. The parameters used to generate this example are  $p_{0i}/p_{0e} = 11$ ,  $T_e = 8.57 \times 10^6 \text{ K}$ ,  $T_i = T_e/10$ , and  $\beta = 10^{-3}$ , and for AB Dor stellar parameters. The co-rotation radius and source surface are shown by the black and red dashed lines, respectively. Note that in panel (b), the black dashed line is specifically for the equatorial co-rotation radius.

pressure. With the field embedded within the equatorial plane, the pressure is constant at a fixed radius. Thus, loops in the equatorial plane are slightly thinner (for a given loop summit height) than their counterparts that are aligned with the rotation axis, since they must support slightly more mass along the field line.

### 3.3 Comparison between a pure dipole and a dipole with a source surface

A dipole magnetic field that becomes radial at the source surface can also be applied in this model. In Fig. 5, a dipole external field with source surface set at  $3.8R_*$  is used. Solving for the cooled loops yields the classic height–width curve found in previous models (Jardine & Cameron 1991; Jardine & van Ballegooijen 2005; Waugh & Jardine 2019) and in Fig. 4. It is reassuring that the results found here do not differ in behaviour from the previous model. Even with the addition of the source surface, the results are qualitatively the same. Whilst the previous work focused solely on the field embedded within the equatorial plane, the same behaviour is found for a field perpendicular to this.

## 4 PROMINENCE MASS DISTRIBUTIONS

### 4.1 The pure dipole

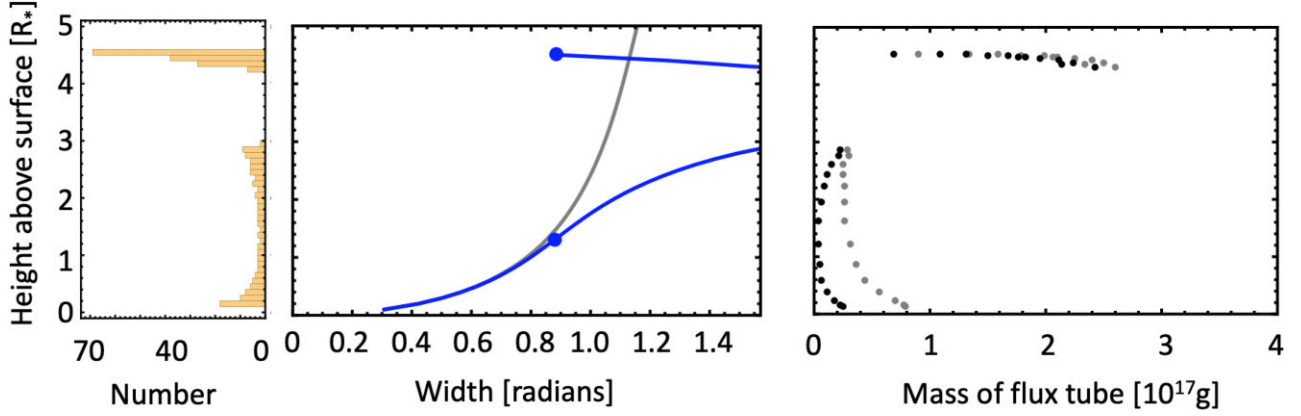
In Section 3, we investigated the shape of loops in a family of cooled solutions, compared to the externally applied field. In this section, we investigate the mass associated with cooled solutions, and how this varies across a family.

Fig. 6 shows a height–width plot (middle panel) for a pure dipolar field, alongside a histogram showing the distribution of the number of solutions at a given height (left panel) and the mass of a flux tubes with height (panel furthest right). The histogram is created by sampling along the height–width curve at intervals of 0.1 rad in width. Due to the flat top of the height–width plot, where small changes in height result in large alterations in loop width, there is a large peak in the number of solutions at the largest heights.

The shapes of the height–width curves are determined by the chosen parameters, a detailed discussion is given in previous papers (Jardine & Cameron 1991; Jardine & van Ballegooijen 2005) but a brief description is given here. The shape of any cooled solution is determined by force balance. The magnetic tension force always acts approximately towards the stellar centre whilst the gradient of the magnetic pressure always acts outwards. The third force present is the buoyancy  $(\rho_e - \rho_i)g$ , which can act inwards or outwards. Inside co-rotation, the gravitational acceleration acts inwards ( $g$  is negative) whilst outside co-rotation, it acts outwards ( $g$  is positive). Whether a loop is overdense or underdense will then determine if the buoyancy force acts inwards or outwards. As the cooled solutions are at a lower temperature than the background field, the solutions at very low or very large heights are denser than the background field. However, around the co-rotation radius they are less dense than the environment, i.e. the loops are underdense. This means these solutions expand, compared to the external field, and this leads to the deviation of the cooled height–width curve compared to the external field, seen in Fig. 6. At some heights, there are no solutions because the shape required to maintain force balance would require the footpoints to be positioned on the other side of the star. At very large heights above the surface, the buoyancy force is strong enough (and outwardly pointing) to balance the inward magnetic tension force, and solutions can be found on an upper branch. With a different choice of parameters, such as a stronger magnetic field, it is possible to find a family of solutions that give one continuous curve.

The right-hand plot in Fig. 6 shows the mass of a flux tube against height of the field line summit. Recall that here the flux tube is constructed around the cooled field line, as shown in Fig. 2. The grey points show the total mass enclosed within the flux tubes, and the black points show the mass above  $r = 0.8r_{\text{summit}}$ . The mass is scaled to observed AB Dor prominence masses of  $10^{17} \text{ g}$  (Cameron & Robinson 1989a). Flux tubes at low heights show masses that are on the order of magnitude of those observed on AB Doradus, however the majority of this mass is found at the footpoints of the flux tube, which can be seen from the corresponding black points. At large heights, the mass within the flux tube is concentrated at the summit, and thus the black and grey points grow closer together.

There are two types of loops: low-lying loops that are close to the stellar surface and below the co-rotation radius (solar-like prominences) and tall loops above the co-rotation radius (slingshot prominences). The solar-like prominences may hold the same order of magnitude of mass as the slingshot prominences, however they are ‘foot heavy’ rather than summit heavy. If or when the loops become unstable, the material in the solar-like prominences would simply



**Figure 6.** Left-hand panel: histogram showing the distribution of the number of loops with height. Middle panel: the height–width plot for the cooled solutions (blue) and external pure dipole field (grey). The two blue dots represent two cooled solutions with the same loop width but different heights. Right-hand panel: flux tube mass against loop height, shown in units of a typical AB Doradus prominence (as determined by observations). Grey represents the total flux tube mass and black shows the mass of the top 80 per cent of the loop.

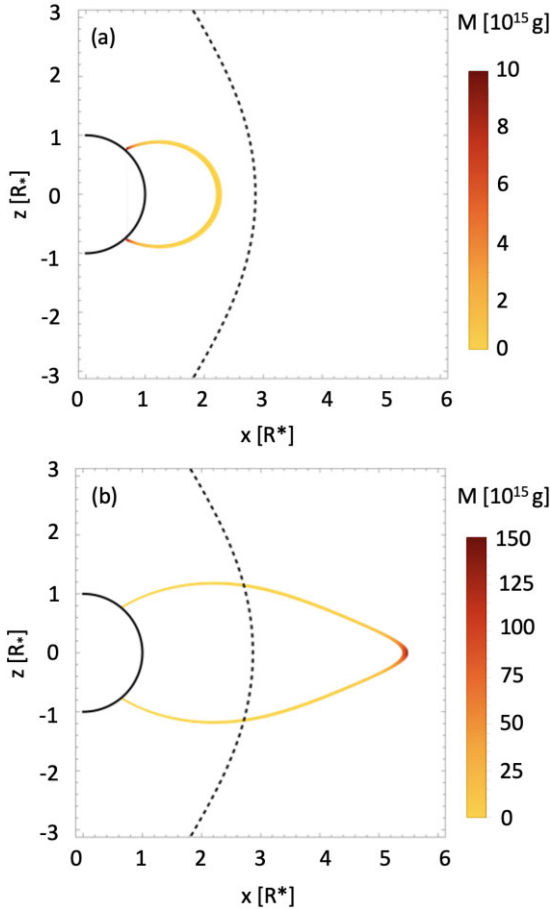


**Figure 7.** Example loops with the same width (1.76 rad) but different heights. The parameters used to generate this example are  $p_{0i}/p_{0e} = 11$ ,  $T_e = 8.57 \times 10^6 \text{K}$ ,  $T_i = T_e/10$ ,  $\beta = 10^{-3}$ , and  $r_s = 3.8R_*$ , and for AB Dor stellar parameters (as mentioned previously). The co-rotation radius is shown by the black dashed line.

fall back to the surface, whilst material in the slingshot prominences would be ejected from the star and into the stellar system. Fig. 7 shows an example of the field line shapes for a solar-like prominence

and slingshot prominence, coloured by the associated mass along the field line.

## 5 SYNTHETIC $H\alpha$ SPECTRA

### 5.1 Plotting the stacked time-resolved spectra of $H\alpha$ lines

Synthetic stacked time-resolved spectra of  $H\alpha$  lines are plotted for a selection of loops. In sum, 10 loops are randomly selected in height from the height–width plots and are then randomly assigned a longitude ( $\phi$ ) value. In the case of the field structures where the magnetic axis is aligned with the rotation pole, the  $\phi$ -value of the loop summit can take any value between 0 and  $2\pi$ . When we compare results to a dipole field that is embedded within the equatorial plane,  $\phi$  is restricted to a choice of two values spaced  $\pi$  radians apart to ensure a dipole structure of the field remains. For simplicity they are assigned to either  $\phi = 0$  or  $\pi$ .

The spectra shown are assuming these model prominences are on the star AB Doradus, with stellar parameters;  $R_* = 0.96 R_\odot$ ,  $M_* = 0.87 M_\odot$ ,  $P = 0.5148 \text{ d}$  (Strassmeier 2009), and an inclination of  $60^\circ$ .

The velocity of the material in the prominence as it co-rotates with the star is determined by

$$v = \Omega_* r_{\text{FT}} \sin \theta_{\text{FT}} \sin(\phi_{\text{FT}} - \phi_0), \quad (20)$$

where  $r_{\text{FT}}$  and  $\theta_{\text{FT}}$  are the radius and the colatitude of the flux tube element, and  $\phi_{\text{FT}}$  is the longitude.  $\phi_0$  is the longitude of the observer as the star rotates.

We calculate the line-of-sight velocity ( $v_{\text{los}}$ ) in order to produce  $H\alpha$  spectra as would be seen by an observer on Earth:

$$v_{\text{los}} = v \sin i. \quad (21)$$

The line-of-sight velocity is calculated for each segment of an individual loop, over multiple rotations of the star (various  $\phi_0$  values). This is repeated for all randomly selected loops.

Absorption tracks are then easily calculated from the line-of-sight integral  $I_a = I_0 e^{\int_0^3 -\kappa \rho ds}$ . Prominences that lie beyond the limb of the star can also scatter photons into the observer’s line of sight (although the geometric dilution factor of  $(r_*/2r)^2$  makes such emission very faint). We none the less show the path of such emission tracks for completeness.

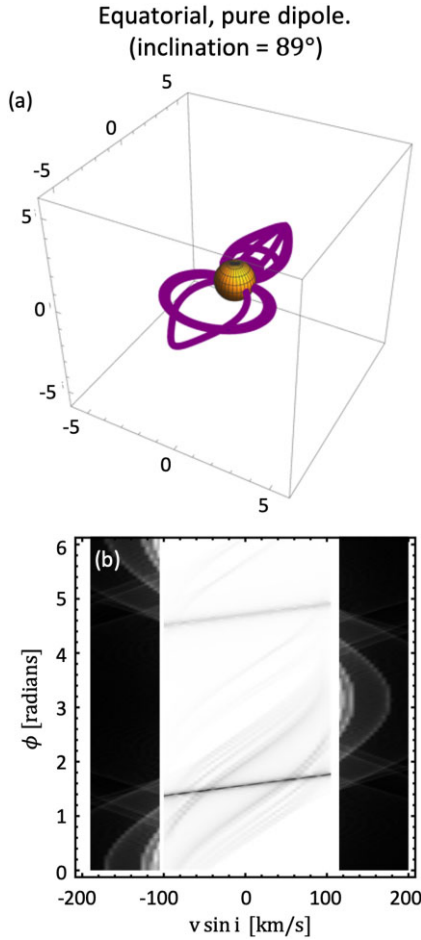


**Figure 8.** (Panel a) Example field lines and (panel b) the associated  $H\alpha$  dynamic spectrum, for the equatorial case and stellar inclination of  $89^\circ$ . The intensity is shown by the colour, with colour tables reversed outside  $v \sin i$  compared to inside. The colour is normalized to the maximum intensity value. The field lines are shown in blue, with sections of the field line that contribute to absorption shown in purple.

## 5.2 The equatorial dipole

Fig. 8 shows the field structure and generated  $H\alpha$  spectrum for a pure dipole field structure embedded within the equatorial plane. The dynamic spectrum shows the tracks that these loops would follow if observed in  $H\alpha$ , with the colour table reversed outside  $v \sin i$  compared to inside to replicate emission rather than absorption. Here the star is given an inclination close to  $90^\circ$ , i.e. the observer lies in the equatorial plane. The sections of the field lines that would be visible in absorption are highlighted in purple. In Fig. 9, the inclination of the star is altered to  $60^\circ$ , similar to that of AB Doradus. The associated  $H\alpha$  spectra are shown in panel (b) of these figures. The low-lying features transit the disc slowly and thus create steep trails. Any feature well above the stellar surface produces a flat trail, since it will transit the disc very quickly.

The importance of the stellar inclination becomes apparent between these two cases. In (a) of Figs 8 and 9, the sections of the field lines that cross the stellar disc are shown in purple. For loops of low heights, the solar-like prominences, the field lines will always cross the stellar disc. However for taller loops that host slingshot prominences, the summits no longer transit the disc once the inclination is set to  $60^\circ$ . In fact, for loops with very large summit

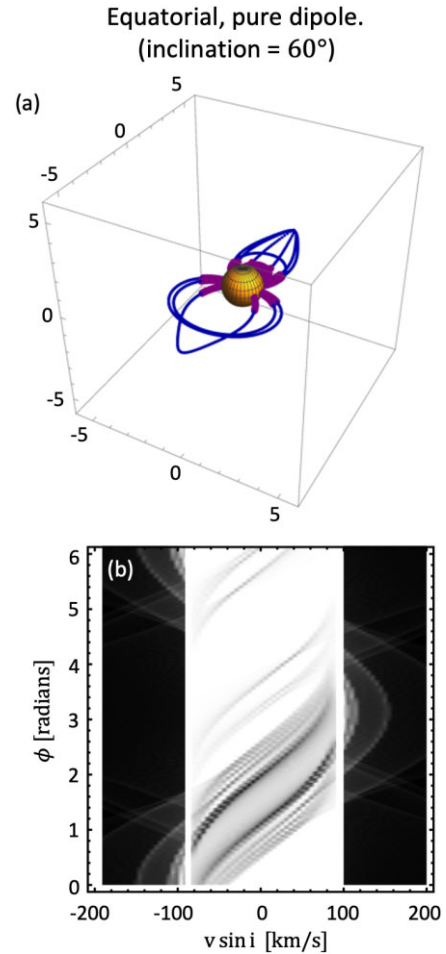


**Figure 9.** (Panel a) Example field lines and (panel b) the associated  $H\alpha$  dynamic spectrum, for the equatorial case and stellar inclination of  $60^\circ$ . The intensity is shown by the colour, with colour tables reversed outside  $v \sin i$  compared to inside. The colour is normalized to the maximum intensity value. The field lines are shown in blue, with sections of the field line that contribute to absorption shown in purple.

heights, there is only a very narrow range of inclinations for which they will transit the disc.

The difference is also seen in the  $H\alpha$  dynamic spectra. In absorption, the fast travelling dark feature in Fig. 9, corresponding to the dense loop summits of the tallest loops, is no longer present in Fig. 8. The dense footpoints are present in both cases, since they always transit the disc. In emission, the loop summits of the very tall loops are not visible due to their large heights above the surface. Areas of the loops close to the stellar surface are present in emission since more star light reaches them, thus they re-emit enough to be seen in emission.

For low-lying loops in this case, there are two absorption features per loop corresponding to the two dense footpoints. For tall loops in this case, there are up to three absorption features per loop: the two dense footpoints and the dense summit. The footpoints in all cases are symmetric in the spectra, since the loops themselves are symmetric in shape. There are two groups of features, one centred about  $\phi = \pi/2$  (the loop group on the right-hand side of the field line plots) and one centred about  $\phi = 3\pi/2$  (the loops on the left-hand side of the field line plots). This is a constraint of having a dipole



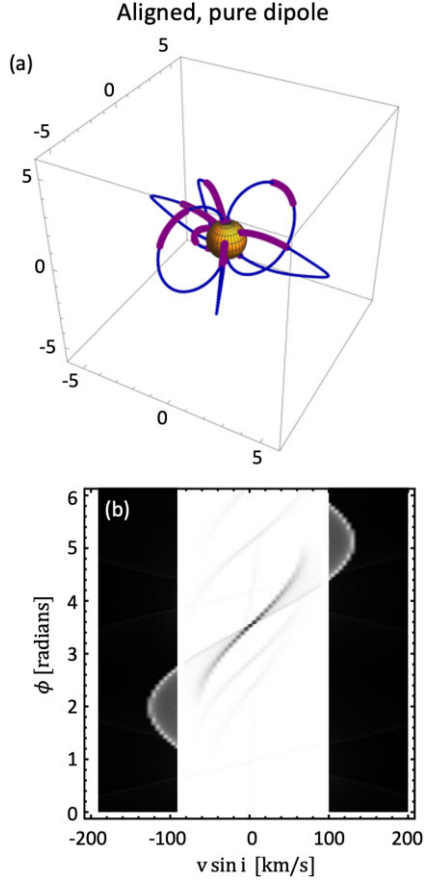


**Figure 10.** (Panel a) Example field lines and (panel b) the associated  $H\alpha$  dynamic spectrum, for the aligned case and stellar inclination of  $60^\circ$ . The intensity is shown by the colour, with colour tables reversed outside  $v \sin i$  compared to inside. The colour is normalized to the maximum intensity value. The field lines are shown in blue, with sections of the field line that contribute to absorption shown in purple.

field embedded within the equatorial plane, where the two lobes of the dipole must be  $\pi$  radians apart.

The absorption is dependent on the total density in the line of sight. Because in this method each flux tube is built around its field line independently of the other cooled field lines present, the footpoints are particularly dense in the  $H\alpha$  spectra. The footpoints may overlap and this can lead to the local density being counted multiple times.

### 5.3 The aligned dipole

Fig. 10 shows the field lines and synthetic  $H\alpha$  dynamic spectrum for the aligned dipole. The stellar inclination is still set at  $60^\circ$ . There are now features at a range of phases, since the loop summits are not restricted to being  $\pi$  radians apart as they were in the equatorial case. Once again, the loop sections that transit the stellar disc are shown in purple in Fig. 10(a). The loop summits of tall loops never transit the disc as they are still within the equatorial plane, so can never be seen in absorption, as was the case in Fig. 9. The difference now is that, with the field lines aligned with the rotation axis, only one side of the loop can transit the disc. There is no longer symmetry in the  $H\alpha$  trails for a given field line, as only one footpoint transits the disc rather than both. Each loop will now contribute one slow-moving feature to the spectrum (a dense footpoint) and could contribute a fast-moving feature for the loop summit, depending on its height.

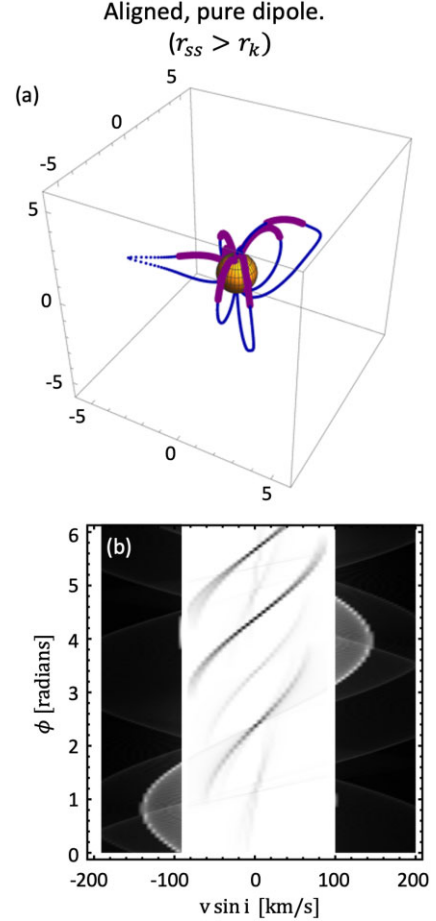


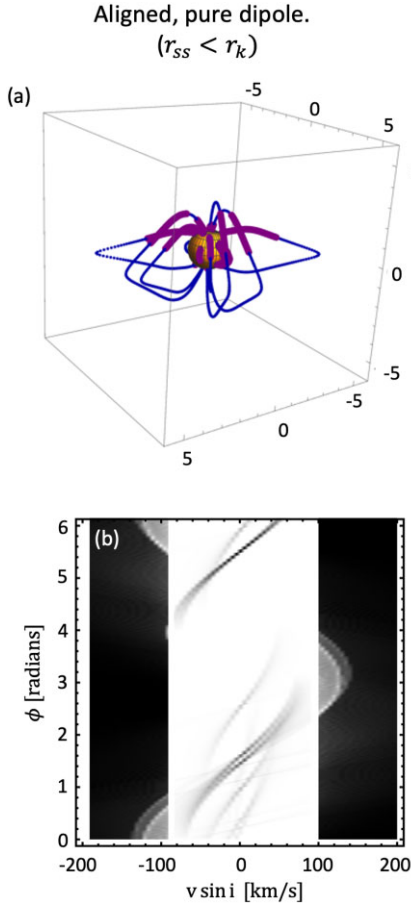
**Figure 11.** (Panel a) Example field lines and (b) the associated  $H\alpha$  dynamic spectrum, for an aligned dipole with:  $r_{ss} = 3.8R_*$ ,  $r_k = 2.8R_*$ , and stellar inclination of  $60^\circ$ . The intensity is shown by the colour, with colour tables reversed outside  $v \sin i$  compared to inside. The colour is normalized to the maximum intensity value. The field lines are shown in blue, with sections of the field line that contribute to absorption shown in purple.

There is only one loop in this sample for which the loop summit is visible in absorption, and also in emission. This low-lying loop, centred around  $\phi = \pi$  radians, is footpoint heavy. This can be seen in the absorption feature by the fact that the flattest part of the feature is not as dark as the slow-moving part. However, in general most loops are only faintly seen in absorption and are too far from the stellar surface to be present in emission.

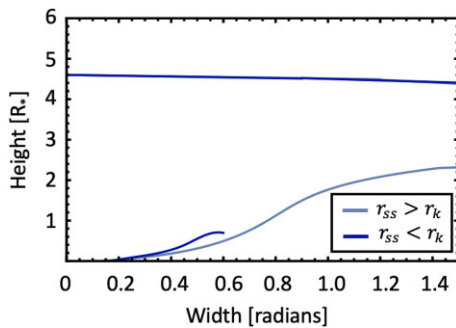
### 5.4 The addition of a source surface

Fig. 11 shows the field lines and synthetic  $H\alpha$  dynamic spectrum for the aligned dipole with source surface above the co-rotation radius, at  $r_{ss} = 3.8R_*$ . Fig. 12 shows the same for a source surface below the co-rotation radius, at  $r_{ss} = 1.8R_*$ . Again, the stellar inclination is set at  $60^\circ$ . In both cases, the  $H\alpha$  trails show similar behaviour to the pure dipole, which is to be expected since these field structures are simply adapted versions of the aligned dipole. In both cases, the summits of the tallest loops are not visible in absorption, and only one footpoint transits the disc.

With the source surface above the co-rotation radius, there are a variety of loop shapes. As the loops are selected at random from the height–width curves, it would have been possible for the sample



**Figure 12.** (Panel a) Example field lines and (panel b) the associated H $\alpha$  dynamic spectrum, for an aligned dipole with:  $r_{ss} = 1.8R_*$ ,  $r_k = 2.8R_*$ , and stellar inclination of  $60^\circ$ . The intensity is shown by the colour, with colour tables reversed outside  $v \sin i$  compared to inside. The colour is normalized to the maximum intensity value. The field lines are shown in blue, with sections of the field line that contribute to absorption shown in purple.



**Figure 13.** Height–width curves showing the family of solutions for the source surface above and below co-rotation.

to have had less variation; however, the shape of the height–width curves determines which loop shapes are possible. When the source surface is placed below co-rotation, the height–width curve has far fewer solutions at low heights, as seen in Fig. 13. This results in much less variation in the possible loop shapes. Whilst the height–width curves look very different at low heights, they are identical to the eye at large heights. At large heights, the loop shape is determined by the balance of the pressure variation and magnetic tension forces,

since the magnetic pressure term is small here. This means that the maximum height of possible solutions is determined by the gas pressure, which, in turn, is determined by the stellar parameters. Thus, the maximum attainable height of a cooled solution is the same between Figs 10, 11, and 12.

The H $\alpha$  dynamic spectrum of Fig. 11 shows this variety of loops despite the loop summits not being visible in absorption. The faint features close to line centre are the footpoints of the tall but wide loops, with their summits being very faintly visible in emission. An example can be seen centred on  $\phi = 1$  or 5 rad. Their footpoints pass slowly through the spectrum (i.e. they have steep gradients) and they have low  $v \sin i$  values due to their position on the surface – they lie closest to the poles, meaning there is less of the stellar disc for them to traverse than a feature on the equator of the disc. The feature centred at  $\phi = 2.5$  rad has a dark footpoint and a fainter summit, which can also be seen faintly in emission. This loop has its summit very close to the co-rotation radius. There is little material at this loop’s summit to absorb, due to the minimum in gas pressure that is found here.

The very dark feature centred around  $\phi = 4.5$  rad is a very low-lying loop, as is the feature centred around  $\phi = 5.5$  rad. All parts of these loops transit the disc, and therefore are present in absorption. Without the knowledge of the associated field line shapes, it would be difficult to tell them apart from the footpoint trails of taller loops, for example the absorption feature centred on  $\phi = 3.5$  rad. This feature corresponds to the tallest and thinnest loop, seen on the left-hand side of Fig. 11(a). Only the footpoint of this loop is visible in absorption, which looks very similar to the features from the low-lying loops previously mentioned, albeit fainter.

Choosing a field structure with the source surface set below the co-rotation radius results in a similar H $\alpha$  dynamic spectrum to previously in absorption, with differences appearing in emission. The shape of the height–width curve for this field structure forces most loops selected to lie on the upper branch, i.e. well above the co-rotation radius. These tall loops have very similar heights to each other, though their widths may take a wide range of values. In this sample there is a selection of tall, wide loops; tall, thinner loops and four low-lying loops. These low-lying features centre on this spectrum around  $\phi = 1.5$  and 5.5 rad. These are the slowest crossing and darkest features, and brightest emission features. Features from the tall, wide loops can be seen at  $\phi = 0.1, 0.5, 1$ , and 1.2 rad. Few of these types of loop were present in the previous case (Fig. 11), but these loop types are more common here due to the shape of the height–width curves. Fig. 12(a) also shows that for these tall but wide-field lines, sometimes the section of the field line that transits the disc may be broken into two sections. Tall, thin loops correspond to the absorption features at  $\phi = 1, 2.5$ , and 6 rad. Only the footpoint of these loops is visible in absorption, creating fast-moving features close to line centre. The summit of these loops can not be seen in absorption or in emission. The emission is the biggest change between Figs 11(b) and 12(b). This is caused by the change in shape of the loops, since now the taller loops are bloated, meaning that the distance from any location on a field line from the centre of the star is greater. Thus, less starlight reaches the point than in the previous case.

### 5.5 Absorption trails alone can not tell us the field structure

Overall, the H $\alpha$  trails look similar across the field structures applied here. The distinction between an equatorial dipole and aligned dipole is the most apparent, though the distinction between a pure dipole and one with a source surface is much more subtle. With the field

structure to directly compare to, one can disentangle which loops cause which trails, but looking at the  $H\alpha$  spectra alone it is not so clear what shaped field line is responsible for a given trail. An absorption feature from Fig. 12(b) for example would seem just as reasonable on the spectra of Fig. 11(b) or 10(b).

Different types of loops cause different trails in the spectra, although with multiple loops combined into a single spectrum it can be difficult to disentangle this information and associate the absorption/emission with a specific loop structure:

- (i) Very low-lying loops have close together footpoints (trails that are thin in  $\phi$ ) and the density from footpoint to summit may be similar, resulting in a similar absorption intensity across the feature.
- (ii) Loops that are ‘bloated’, with their summits around the co-rotation radius, have large footpoint separations. They have heavy footpoints and empty summits, thus their footpoints are dark in the absorption spectra and the features are wide in  $\phi$ . The summits show little absorption.
- (iii) Tall loops, well above co-rotation, have close together footpoints and dense summits. Their features are less wide in  $\phi$  than bloated loops, and have high absorption at the footpoints and summit, showing three dark stripes in the  $H\alpha$  trails.

The  $H\alpha$  trails between the different field structures do look somewhat different:

- (i) In the equatorial case material can only collect at two phases that are centred  $\phi = \pi$  radians apart, due to the constraints of the loop summit locations. Features are symmetric about their centre, since for each loop both legs of the field line are seen.
- (ii) Going from the equatorial to aligned cases, the trails of individual loops look different as now only one field line leg transits the disc. Features may now form at any phases, spreading the individual features out in phase.
- (iii) With a source surface included above the co-rotation radius the spectrum looks very similar to the pure dipole, and the absorption spectrum of the source surface below co-rotation.
- (iv) With a source surface included below the co-rotation radius, most loops are very tall. This restriction is caused by the shape of the height–width plot. This means that most of the mass is never seen in absorption as it never transits the disc. This creates more lines in the emission spectrum than for the previous cases.

Whilst there are slight differences between the cases shown here and between the different loop types mentioned, ultimately it is very difficult to tell them all apart without the field structure to guide understanding. This can not be done so easily with observations. Field structures of stars can be generated from ZDI maps, however these rely on assumptions to determine the boundary conditions of the spherical harmonics and in turn produce a field structure. Thus, the field structures generated from observations may not fully reflect the true stellar field. Here, since the field was determined prior to the  $H\alpha$  structure, it is a known quantity to refer back to when examining the spectra. However, this does mean that the observed features can be very easily replicated since many field structures can generate similar trails. This implies that prominences can form over a wide range of parameters and thus are likely to be common features on these stars. This is consistent with observations of prominences on many different stars.

## 6 CONCLUSIONS

This paper has expanded upon a previous model that generated prominence bearing field lines for field embedded within the equa-

torial plane (Waugh & Jardine 2019). A background field is applied and within this the shapes of all possible cool loops of a chosen temperature and pressure are determined. These cooled field lines are mechanical equilibria, and are mass loaded by the dense material that they must support. This causes them to take an adjusted shape from the external field. Here, we have expanded the model to account for a more general field structure that is aligned with the rotation axis. We investigate the difference between the equatorial case and the aligned case, which are the two idealized extremes. We make estimates for prominence masses for the aligned dipole field structure, and generate  $H\alpha$  trails for the equatorial dipole, aligned dipole and aligned dipole with an added source surface.

Loop shapes are qualitatively similar to the previous paper, with slight variations in shape caused by the latitudinal dependence of the effective gravity force. This causes the pressure to vary with latitude, reaching a maximum in the equatorial plane (where it is independent of longitude). This suggests that the previous model, though very simplified, is robust in the behaviour it produces. The loop shapes for the previous method, the equatorial case, and the new, aligned dipole all show the same behaviour. The height–width curves shown in Fig. 4 are the same overall shape, with the difference between the two becoming apparent at large heights. The dominating pressure term at these heights causes the aligned loops to be wider than their equatorial counterparts. This is caused by the pressure variation, shown in Fig. 3. In order to support the same mass as the aligned loops, the equatorial loops must take a smaller radius of curvature. Despite this, the maximum loop height is identical in the two cases since it depends on the stellar parameters alone (Jardine & van Ballegooijen 2005).

Estimates of prominence masses are shown in Section 4 for the aligned dipole. The flux tube masses are calculated for a family of solutions and shown in Fig. 6. The solutions all yield masses in the range  $(0.5\text{--}2.6) \times 10^{17}\text{g}$ . This is similar to the prominences observed on AB Doradus with masses of  $(2\text{--}6) \times 10^{17}\text{g}$  (Cameron et al. 1990). There are two types of solution; low-lying loops that are close to the stellar surface and below co-rotation (solar-like prominences) and tall loops above the co-rotation radius (slingshot prominences). Whilst the masses of flux tubes at very low heights lie within the same order of magnitude as the tall thin prominences, they contain very little mass at their summits and are ‘footpoint heavy’. On the other hand, the tallest loops carry almost all of their mass at their summits. Prominence masses drop from the surface to the co-rotation radius as the gas pressure decreases to a minimum. The flux tubes at co-rotation show the lowest masses in the sample. Masses for prominences on the top branch are much larger, but decrease with height. Although the gas pressure is still increasing with height, the volume of the flux tube is quickly decreasing as the loops are stretched taller and thinner. If these loops became unstable, the material in the solar-like prominences would likely fall back to the surface since it is below the co-rotation radius. It could be ejected from the star if it was actively propelled to do so, such as during a coronal mass ejection (CME). The material in the slingshot prominences, forming beyond the co-rotation radius, would be ejected from the star and into the stellar system.

We generate synthetic  $H\alpha$  trails for the field structures examined here, which show the prominence bearing field lines in absorption and potentially in emission, although we caution that the intensity in emission is rarely high enough for this to be detectable. The trail appearances depend on the field structure and the stellar inclination. For a star with an inclination of  $90^\circ$ , viewed in its equatorial plane, there would be a clear distinction between the  $H\alpha$  traces of an equatorial and an aligned dipole with the slingshot prominences still

being visible as absorption features in the spectra. The magnetic fields of these stars can not be mapped by ZDI because it is impossible to distinguish between the two hemispheres of the star. However, it is possible to observe in  $H\alpha$  for these stars. Thus, they could be used to infer information about the tilt of the dipole axis. For most of the spectra shown here, the stellar inclination is set to  $60^\circ$ , similar to the value for AB Doradus. At this inclination, the summits of tall loops are not visible in absorption since they lie far above the surface in the equatorial plane, and can never transit the stellar disc. Whilst low-lying loops may be visible as emission trails, this is less likely for tall loops due to their large heights above the surface. In theory the footpoints of loops are easy to see in absorption since they will almost always transit the disc and they are dense. In practice, they may be more difficult to see in the observations since they transit slowly, and the star may not be observed for long enough for a detectable absorption trail to be found. In the equatorial case with an inclination of  $90^\circ$ , there are often two or three dark lines for a given field line in absorption (two for the footpoints and one for a dense summit). With a smaller inclination of  $60^\circ$ , these are reduced to one or two lines, since one hemisphere can never be seen and both footpoints and the summit cannot all transit the disc. The ease with which the observed  $H\alpha$  dynamic spectra can be reproduced by a wide variety of loop structures certainly explains the large number of absorption transients commonly seen. It is clear from these models also that a large fraction of the prominence mass is unlikely to be detected in absorption as it never transits the disc.

## ACKNOWLEDGEMENTS

The authors acknowledge support from STFC consolidated grant number ST/R000824/1.

## DATA AVAILABILITY

The research data listed in the tables here can be accessed at: <https://doi.org/10.17630/1d412b50-eb71-4ecd-aa86-fc9769bd215b> (Waugh & Jardine 2022).

## REFERENCES

- Aarnio A. N., Matt S. P., Strassun K. G., 2012, *ApJ*, 760, 1
- Barnes J. R., Cameron A. C., James D. J., Donati J.-F., 2000, *MNRAS*, 314, 162
- Barnes J. R., Cameron A. C., James D. J., Steeghs D., 2001, *MNRAS*, 326, 1057
- Bourrier V., Lecavelier des Etangs A., Ehrenreich D., Tanaka Y., Vidotto A., 2016, *A&A*, 591, 14
- Byrne P. B., Eibe M. T., Rolleston W. R. J., 1996, *A&A*, 311, 651
- Cameron A. C. et al., 1999, *MNRAS*, 308, 493
- Cameron A. C., Robinson R., 1989a, *MNRAS*, 236, 57
- Cameron A. C., Robinson R., 1989b, *MNRAS*, 238, 657
- Cameron A. C., Woods J., 1992, *MNRAS*, 258, 360
- Cameron A. C., Duncan D., Ehrenfreund P., Foing B., Kuntz D., Penston M., 1990, *MNRAS*, 247, 415
- Cang T.-Q. et al., 2020, *A&A*, 643, 16
- Climent J. B., Guirado J. C., Azulay R., Marcaide J. M., Jauncey D. L., Lestrade J. F., Reynolds J. E., 2020, *A&A*, 641, A90
- Collier Cameron A., 1996, *Stellar Surf. Struct.*, 176, 449
- Collier Cameron A., Jardine M. M., Donati J. F., 2002, in Favata F., Drake J. J., eds, *ASP Conf. Ser. Vol. 277, Stellar Coronae in the Chandra and XMM-NEWTON Era*. Astron. Soc. Pac., San Francisco, p. 397
- Cranmer S. R., 2017, *ApJ*, 840, 114
- Donati J.-F., Mengel M., Carter B. D., Marsden S., Cameron A. C., Wichmann R., 2000, *MNRAS*, 316, 699
- Doyle J., Cameron A. C., 1990, *MNRAS*, 244, 291
- Dunstone N. J., Barnes J. R., Cameron A. C., Jardine M., 2006a, *MNRAS*, 365, 530
- Dunstone N. J., Cameron A. C., Barnes J. R., Jardine M., 2006b, *MNRAS*, 373, 1308
- Eibe M., 1998, *A&A*, 337, 757
- Ferreira J., 2000, *MNRAS*, 316, 647
- Fichtinger B., Güdel M., Mutel R., Hallinan G., Gaidos E., Skinner S., Lynch C., Gayley K., 2017, *A&A*, 599, A127
- Hall J. C., Huenemoerder D. P., Ramsey L. W., Buzasi D. L., 1990, *A&A*, 358, 610
- Hussain G. A. J., Jardine M., Cameron A. C., 2001, *MNRAS*, 322, 681
- Hussain G. A. J., van Ballegoijen A. A., Jardine M., Cameron A. C., 2002, *ApJ*, 1
- Jardine M., Cameron A. C., 1991, *Sol. Phys.*, 131, 269
- Jardine M., Cameron A. C., 2019, *MNRAS*, 482, 2853
- Jardine M., van Ballegoijen A., 2005, *MNRAS*, 361, 1173
- Jardine M., Cameron A. C., Donati J.-F., Pointer G. R., 2001, *MNRAS*, 324, 201
- Jardine M., Wood K., Cameron A. C., Donati J.-F., Mackay D. H., 2002a, *MNRAS*, 336, 1364
- Jardine M., Cameron A. C., Donati J.-F., 2002b, *MNRAS*, 333, 339
- Kolbin A., Tsymbal V., 2017, *Astron. Rep.*, 61, 521
- Landstreet J. D., Borra E. F., 1978, *ApJ*, 224, L5
- Leitzinger M., Odert P., Zaqarashvili T. V., Greimel R., Hanslmeier A., Lammer H., 2016, *MNRAS*, 463, 965
- Lim J., White S., 1996, *ApJ*, 462, L91
- Massi M. et al., 2008, *A&A*, 480, 489
- Panagia N., Felli M., 1975, *A&A*, 39, 1
- Parker E. N., 1975, *ApJ*, 201, 494
- Petit V. et al., 2013, *MNRAS*, 429, 398
- Reville V., Brun A. S., Strugarek A., Matt S., Bouvier J., Folsom C., Petit P., 2015, *ApJ*, 814, 99
- See V. et al., 2018, *MNRAS*, 474, 536
- Skelly M., Donati J.-F., Bouvier J., Grankin K., Unruh Y., Artemenko S., Petrov P., 2010, *MNRAS*, 403, 159
- Skelly M. B., Unruh Y. C., Cameron A. C., Barnes J. R., Donati J.-F., Lawson W. A., Carter B. D., 2008, *MNRAS*, 385, 708
- Skelly M. B., Unruh Y. C., Barnes J. R., Lawson W. A., Donati J.-F., Cameron A. C., 2009, *MNRAS*, 399, 1829
- Spruit H. C., 1981, *A&A*, 98, 155
- Stauffer J. et al., 2017, *ApJ*, 153, 34
- Strassmeier K. G., 2009, *A&AR.*, 17, 251
- Van den Oord G., 1998, in Webb D. F., Schmieder B., Rust D. M., eds, *ASP Conf. Ser. Vol. 150, New Perspectives on Solar Prominences*. Astron. Soc. Pac., San Francisco, p. 251
- Van den Oord G., Doyle J., 1997, *A&A*, 319, 578
- Vida K. et al., 2016, *A&A*, 590, 1
- Vidotto A. A., Bourrier V., 2017, *MNRAS*, 470, 4026
- Vidotto A. A., Jardine M., Opher M., Donati J. F., Gombosi T. I., 2011, in Johns-Krull C. M., Browning M. K., West A. A., eds, *ASP Conf. Ser. Vol. 448, 16th Cambridge Workshop on Cool Stars, Stellar Systems, and the Sun*. Astron. Soc. Pac., San Francisco, p. 1293
- Villadsen J., Hallinan G., Bourke S., Güdel M., Rupen M., 2014, *ApJ*, 788:112, 1
- Villarreal D'Angelo C., Jardine M., See V., 2018, *MNRAS*, 475, 25
- Villarreal D'Angelo C., Jardine M., Johnstone C., See V., 2019, *MNRAS*, 485, 1448
- Watson C., Steeghs D., Dhillon V., Shahbaz T., 2007, *Astron. Nachr.*, 328, 813
- Waugh R., Jardine M., 2022, *MNRAS*, available at: <https://doi.org/10.1093/mnras/stac1698>
- Waugh R. F. P., Jardine M. M., 2019, *MNRAS*, 483, 1513
- Waugh R. F. P., Jardine M. M., Morin J., Donati J.-F., 2021, *MNRAS*, 505, 5104
- Weber E., Davis L., 1967, *ApJ*, 148, 217
- Wood B. E., Muller H. R., Zank G. P., Linsky J. L., Redfield S., 2005, *ApJ*, 628, L143



**APPENDIX A:**

Along the magnetic field, the momentum equation can be simplified to

$$0 = -\nabla p \cdot \hat{s} + \rho \mathbf{g}_e \cdot \hat{s}, \quad (\text{A1})$$

since the Lorentz force is equal to zero.

$$\frac{dp}{ds} = \frac{mp}{K_B T} \left[ \left( -\frac{GM_\star}{r^2} + \omega^2 r \sin^2 \theta \right) \frac{r'}{\sqrt{(r')^2 + r^2}} + \frac{\omega^2 r \sin \theta \cos \theta}{\sqrt{(r')^2 + r^2}} \right]. \quad (\text{A2})$$

Using  $ds = \sqrt{(r')^2 + r^2} d\theta$ , this simplifies to

$$\frac{dp}{d\theta} = \frac{mp}{K_B T} \left[ \left( -\frac{GM_\star}{r^2} + \omega^2 r \sin^2 \theta \right) r' + \omega^2 r^2 \sin \theta \cos \theta \right], \quad (\text{A3})$$

which can be integrated as

$$\int_{p_\star}^{p(r,\theta)} \frac{1}{p} dp = \frac{m}{K_B T} \left[ \int_{R_\star}^{r R_\star} \left( -\frac{GM_\star}{r^2} + \omega^2 r \sin^2 \theta \right) \frac{dr}{d\theta} d\theta + \int_0^{2\pi} \omega^2 r^2 \sin \theta \cos \theta d\theta \right]. \quad (\text{A4})$$

This can be solved to find the gas pressure variation with  $r$  and  $\theta$ , in terms of the loop temperature ( $T$ ) and base pressure ( $p_0$ ):

$$p = p_0 \exp \left[ \frac{m}{K_B T} \left( GM_\star \frac{(1-r)}{r R_\star} + \omega^2 R_\star^2 \sin^2 \theta \frac{(r^2 - 1)}{2} \right) \right], \quad (\text{A5})$$

This paper has been typeset from a  $\text{\LaTeX}$  file prepared by the author.